

Attenuation of Rayleigh waves due to three-dimensional surface roughness: A comprehensive numerical evaluation^a

Georgios Sarris¹, Stewart G. Haslinger^{2,4}, Peter Huthwaite¹, Peter B. Nagy^{3,4} and Michael J. S. Lowe¹

Abstract

The phenomenon of Rayleigh wave attenuation due to surface roughness has been well studied theoretically in the literature. Three scattering regimes describing it have been identified - the Rayleigh (long wavelength), stochastic (medium wavelength) and geometric (short wavelength), with the attenuation coefficient exhibiting a different behaviour in each. Here, in an extension to our previous work, we gain further insight with regard to the existing theory, in three dimensions, using finite element (FE) modelling, under a unified approach, where the same FE modelling techniques are used regardless of the scattering regime. We demonstrate good agreement between our FE results and the theory in all scattering regimes. Additionally, following this demonstration, we extend the results to cases that lie outside the limits of validity of the theory.

1 Introduction

Rayleigh waves exist on the surfaces of elastic solids, at traction-free boundaries. Surfaces of propagation are well known to attenuate the Rayleigh

^aManuscript accepted for publication in JASA - available at <https://doi.org/10.1121/10.0020564>.

¹Department of Mechanical Engineering, Imperial College London, London, SW7 1AY, United Kingdom.

²Department of Mathematical Sciences, University of Liverpool, Liverpool, L69 7ZL, United Kingdom.

⁴Also at: Department of Mechanical Engineering, Imperial College London, London, SW7 1AY, United Kingdom.

³Department of Aerospace Engineering and Engineering Mechanics, University of Cincinnati, Cincinnati, OH 45221, USA.

waves, due to the presence of roughness. Since all solids unavoidably possess a certain degree of roughness [1], it is important to understand how this roughness influences the propagation of Rayleigh waves, especially when attenuation is used as a non-destructive evaluation measure [2–5]. Additionally, good understanding of this phenomenon can lay the groundwork for utilizing it as an efficient method for characterising the degree of roughness of a material, when it is unknown.

There exist multiple theoretical studies that derive expressions predicting the attenuation coefficient of a Rayleigh wave travelling over a rough surface. Some of the most well-known results come from the work in [6] and [7]. In their work the authors derived expressions relating the attenuation coefficient of Rayleigh waves with the frequency f , and the root mean square (RMS) height (δ) and correlation length (Λ) of the surface. The latter two variables are metrics characterising the height of the peaks/troughs of the rough surface, and the spacing between them respectively. The authors show that in the long wavelength limit, known as the Rayleigh regime, the attenuation coefficient is proportional to $\delta^2\Lambda^2f^5$. The results from these authors were obtained using small perturbation methods; in [8], the same power relationships were retrieved using the Rayleigh-Born approximation.

Most of the literature in rough surface scattering focuses on the study of the Rayleigh (long wavelength) regime, which was discussed in the previous paragraph. As the frequency increases, the findings in [7], and later, [9], show that in the stochastic regime (medium wavelength), the attenuation coefficient is proportional to $\delta^2\Lambda^{-1}f^2$. Finally, in the geometric regime (short wavelength), we rely on the findings of our previous work in [10], combined with the dimensional analysis in [11] and the results in [12, 13], where it was shown that the attenuation coefficient is proportional to Λ^{-1} and independent of δ and f .

However, experimental validation of these relationships has proven unfeasible due to a combination of the difficulty in reproducing the required rough surfaces in the real world, and the high attenuation values that they cause, which makes the waves very difficult to detect in experimental investigations. Additionally, the theoretical models require the use of various approximations and mathematical techniques to predict the attenuation coefficient in each

scattering regime, further increasing the complexity in the predictions. In our previous work in [10] we were able to verify the relevant theory in two-dimensional (2D) space, and expand it to roughness combinations beyond its limits of validity. The verification was completed using results from finite element (FE) modelling. FE modelling allowed us to complete the verification across all three scattering regimes under a single, unified approach, as we were able to use the same model regardless of the scattering regime and the roughness parameters. Additionally, physical assumptions beyond the fundamental discretisation of the underlying displacement field, which can be addressed with suitable mesh refinement, are not made during FE modelling - this eliminates any additional assumptions that were made in past theoretical work.

Completing a three-dimensional (3D) study previously was considered not to have been possible due to the computational burden of solving multiple 3D models to determine roughness parameters suitable for our study, as, to our knowledge, there did not exist another FE study that could be used as a reference. Now, having identified particular regions of parameter space that are accessible by our models and that satisfy the theory's requirements, and tuning our models, we extend to three dimensions. The results here both strengthen our findings in [10] and allow us to gain further insight with regard to the theory in [7, 9], in 3D space, eliminating the need for using analogies between the 2D and 3D theories. Additionally, we demonstrate the power relationships between the attenuation coefficient and the surface's statistical parameters and frequency in the geometric regime, which, to our knowledge is relatively unexplored in terms of scattering from rough surfaces; in our 2D work we used an analogy with grain scattering, and dimensional analysis to derive the expected power relationships, however here we are able to investigate this relationship and the analogy directly. Also, following the demonstration in all scattering regimes similarly to [10], we extend our results to regions beyond the postulated limits of validity of the existing theory, showing the capabilities of FE modelling to produce results for a plethora of roughness cases without the relatively low roughness restriction ($\delta/\Lambda < 0.3$), that the theory requires. This advancement in understanding lays the groundwork for either future use of FE modelling for predicting (and correcting for) the attenuation coefficient caused by a given roughness

profile, or an inverted approach, where the attenuation coefficient is used to quantify the surface roughness of a component, without the relatively low roughness restriction imposed by the theory. It is also worth noting that the theory in [7, 9] also predicts a frequency shift caused by the roughness, however, our work here focuses solely on the behaviour of the attenuation coefficient. Dispersion and diffraction effects can be also formulated in the general framework of a “global theory” based on dimensional analysis and similitude, similarly to our 2D work in [10]. From the practical point of view of ultrasonic Non-Destructive Evaluation (NDE), those effects are less significant than the attenuation effect studied in this paper. However, there cannot be any doubt that the numerical technique presented in this paper is suitable to study those effects as well, although sufficiently accurate assessment of weaker effects naturally requires higher numerical accuracy (i.e., higher meshing refinement, smaller time steps and hence more computational power etc.).

This paper is organised as follows: Section 2 presents a summary of the theory used in our work and Section 3 explains the details behind generating the FE models. Then, Section 4 presents the asymptotic power relationships obtained from solving the FE models, between the attenuation coefficient and δ , Λ and f , comparing them with theoretical predictions, and finally, Section 5 summarises the work.

2 Theory

In this section we present a brief summary of the theory used in this work; first we discuss the relevant theory for defining and generating statistically rough surfaces, for later use in our FE models, and subsequently we present the theory and resulting power relationships for describing the behaviour of the attenuation coefficient in the three scattering regimes.

2.1 Rough surfaces

A surface can be thought of as rough when its local height over a reference plane varies with space. There are two statistical parameters with which the roughness of a surface is often mathematically quantified - the RMS height

δ , and correlation length Λ . The former parameter can be thought of as a metric of the height/depth of the peaks and troughs of the surface, while the latter is a measure of the spacing between them.

Let x and y span the plane over which a rough surface exists, and let z be the direction perpendicular to this plane. Since the variation of the height h of a rough surface is a function of the location, the rough profile can be expressed as:

$$z = h(x, y). \quad (1)$$

In our study, we have assumed rough surfaces with a zero mean height, i.e. $\langle h \rangle = 0$, where $\langle \rangle$ denotes spatial and/or ensemble averaging. In this case, δ can be calculated from:

$$\delta = \sqrt{\langle h^2 \rangle}. \quad (2)$$

We have also selected a Gaussian correlation function, $C(x, y)$:

$$C(x, y) = \exp \left[- \left(\frac{x^2}{\Lambda_x^2} + \frac{y^2}{\Lambda_y^2} \right) \right], \quad (3)$$

where Λ_x and Λ_y are the correlation lengths in the x and y directions respectively. The correlation function is a statistical measure of local similarity between points on the surface as a function of the distance between them. In our study, similarly to [7], we selected the same correlation length in both directions, i.e. $\Lambda_x = \Lambda_y = \Lambda$, and hence

$$C(R) = \exp \left(- \frac{x^2 + y^2}{\Lambda^2} \right), \quad (4)$$

where the correlation length Λ is the distance over which $C(R)$ drops to $1/e$ of its initial value, and $R = \sqrt{(x^2 + y^2)}$. The choice of the correlation lengths in the x and y directions to be equal was made because this is a requirement of the theoretical derivations in [7] and [9], into which our work attempted to gain more insight; we expect that a mismatch in the correlation lengths in the two directions could make a significant difference to the attenuation, as we already know that the limiting case of an extrusion in one axis will cause the attenuation results given by the 2D cases we reported previously. Additionally, this is representative of many physical processes where the resulting

surface roughness would be isotropic. We have chosen Gaussian roughness to follow the methodology of our previous work in [10], but also because this roughness has been well studied [1, 14, 15], and also occurs in real scenarios [16–18]. It would have also been possible to generate rough surfaces from real data, similarly to [16] - however, provided that the real roughness is a result of a random process, the power relationships between the attenuation coefficient and δ, Λ and f would not have been different. Also, replicating a real rough surface, that was not generated by a random process, in our FE domain would only provide a direct result for that particular surface and therefore, no comparison with the existing, theoretical models.

The rough surfaces were generated using MATLAB, by implementing the weighted moving average approach discussed in [1, 14, 15]. Under this approach an array of pseudo-random numbers was generated and then converted to an array with correlated numbers, such that the array corresponds to the desired $h(x, y)$ profile. Here, a Tukey window, $w(x)$ was also applied to each row (x direction) of the array as follows:

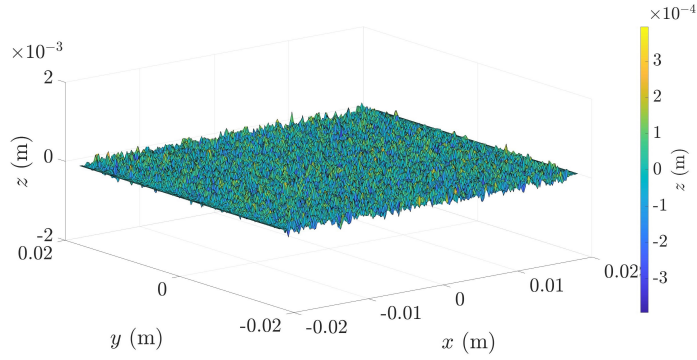
$$w(x) = \begin{cases} 0 & |x| \geq \frac{L}{2} \\ 1 & |x| \leq \frac{L}{2} - \frac{l_w}{2} \\ \frac{1}{2} \left[1 - \cos \left(2\pi \frac{|x| - \frac{L}{2}}{l_w} \right) \right] & \text{otherwise,} \end{cases} \quad (5)$$

where L is the length of the row of the array being windowed, and l_w is the length of the window tapering. For the simulations in this paper $l_w = \frac{L}{10}$ was used. Examples of such rough surfaces, corresponding to rough surfaces in each scattering regime, with the windowing applied, are shown in Figure 1.

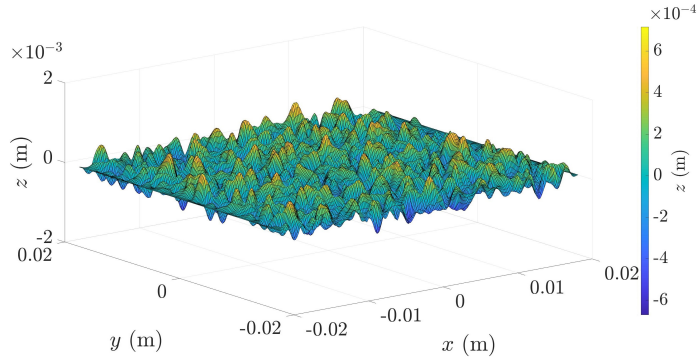
As shown in Figure 1, this method generates a rough surface with smooth peaks and troughs, and the windowing reduces the amplitude of those to zero, at the edges of the rough zone, to ensure a smooth joining with the smooth parts of the FE domain.

2.2 Attenuation coefficient

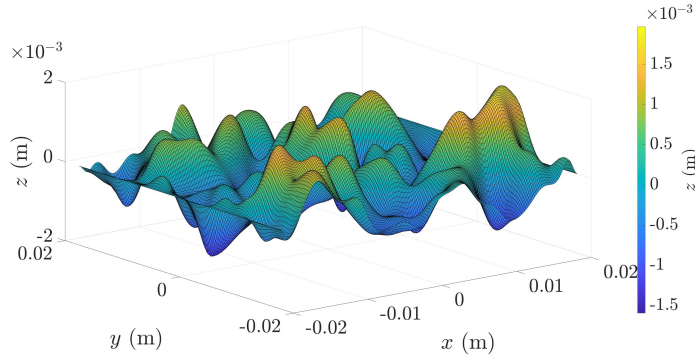
The attenuation of a Rayleigh wave, when it travels over a rough surface can be calculated by [7]:



(a)



(b)



(c)

Figure 1: (Colour online) Examples of 3D rough surfaces generated with the moving average method described in [1, 14, 15]. In (a), $\delta = 100 \mu\text{m}$ and $\Lambda = 250 \mu\text{m}$, in (b), $\delta = 200 \mu\text{m}$ and $\Lambda = 800 \mu\text{m}$ and in (c), $\delta = 600 \mu\text{m}$ and $\Lambda = 3000 \mu\text{m}$. The windowing in Equation (5) has also been applied to each row of the array which contains the z values corresponding to this surface. Each of the surfaces in (a), (b) and (c) are characterised by statistical parameters whose values correspond to the Rayleigh, stochastic and geometric regimes at $f = 1 \text{ MHz}$.

$$l^{-1} = 2 \frac{\delta^2}{\Lambda^2} q \omega_2, \quad (6)$$

where l is the attenuation length, and q is the wavenumber. We use q to denote the wavenumber instead of the usual k , to follow the same notation as in [7], and our previous work in 2D space [10]. The term ω_2 is a function encapsulating the effects of the roughness on the Rayleigh wave, as it contains information about the rough surface, the material and the wave itself. The attenuation length is defined as the length over which the energy of a wave drops to $1/e$ from its initial value. However, in FE simulations it is more straightforward to measure the displacement amplitude of a wave instead of its energy. Given that the energy of a wave is proportional to the square of its displacement amplitude [19, 20], it can be shown that

$$\alpha = \frac{1}{2l}, \quad (7)$$

and therefore,

$$\alpha = \frac{\delta^2}{\Lambda^2} q \omega_2. \quad (8)$$

In [7], the authors show that in the Rayleigh regime (long wavelength), $\omega_2 \propto (\omega\Lambda)^4$, where ω is the angular frequency, and therefore, $\alpha_R \propto \delta^2 \Lambda^2 f^5$, where the subscript R denotes the Rayleigh regime.

In the stochastic regime (medium wavelength), analytical expressions for the behaviour of the attenuation coefficient have been derived in [9]; the authors have shown that as the frequency increases, the $\alpha_R \propto \delta^2 \Lambda^2 f^5$ proportionality becomes $\alpha_S \propto \delta^2 \Lambda^{-1} f^2$, where the superscript S denotes the stochastic regime. This power relationship is also inferred in [7], as the ω_2 function can be seen to vary linearly with $\omega\Lambda$, which, when substituted in Equation (8), yields the same power relationship.

It is worth noting that the power relationships between the attenuation coefficient and the statistical parameters/frequency are expected to be identical between two and three dimensions in the stochastic and geometric regimes. This phenomenon has been discussed in [11], and demonstrated in our work in [10], where we have used 3D theory to predict the 2D power relationships, which we were subsequently able to verify. Therefore, in the geometric

regime, it is expected that $\alpha_G \propto \Lambda^{-1}$, where the subscript G denotes the geometric regime.

A summary of the expected power relationships between α and δ , Λ and f , which our work attempts to demonstrate, is shown in Table 1.

Table 1: Expected theoretical asymptotic power relationships, between the attenuation coefficient and the RMS height, correlation length and frequency.

Regime	Rayleigh	Stochastic	Geometric
Limits	$q\delta < q\Lambda < 1$	$q\delta < 1 < q\Lambda$	$1 < q\delta \ll q\Lambda$
$\alpha(\delta, \Lambda, f)$	$\delta^2 \Lambda^2 f^5$	$\delta^2 \Lambda^{-1} f^2$	Λ^{-1}

3 FE modelling

We now present the methods that we used to generate the FE models. For all FE simulation in this work we used the high-fidelity graphics processing unit (GPU) based FE package Pogo, and visualised our results using PogoPro [21]. Let us assume an FE model, where \mathbf{U} and $\ddot{\mathbf{U}}$ are the matrices containing the displacements and accelerations of the nodes in the FE model. The equation of motion of this model, with no damping, in its finite difference form, which is often used by FE solvers [22], is

$$\mathbf{M} \frac{\mathbf{U}^{s+1} - 2\mathbf{U}^s + \mathbf{U}^{s-1}}{\Delta t^2} + \mathbf{K}\mathbf{U}^s = \mathbf{F}, \quad (9)$$

where \mathbf{M} , \mathbf{K} , and \mathbf{F} are the mass, stiffness, and applied force matrices respectively. The superscript s denotes the s th time step, and Δt is the duration of said time step. Knowledge of the nodal displacements and accelerations in the two previous time steps allows for calculating the displacement at the next time step.

We used the 2D model in our previous work in [10] as a basis for constructing the 3D model for this study. In the 2D model, a rough surface was inserted at the bottom boundary of a rectangular FE domain, with monitor nodes on both sides of it, and a source line, composed of multiple source nodes, further to the left. Source nodes with pre-determined displacements, were used to

excite waves in a model, and monitor nodes measure displacements that are stored by the FE solver and can be used during post-processing. For the initial 3D model with flat surfaces, prior to the insertion of the rough area, we used an “extruded” version of the 2D model, i.e. the rough surface and source lines were converted into rough and source areas respectively, while the monitor nodes were converted into monitor lines. A planar schematic of this configuration is shown in Figure 2. Similarly to our 2D work, the source nodes were chosen to be outside the rough area, to ensure that a clean Rayleigh wave would arrive at the rough area; although placing the source area within the rough region would be more realistic, it would prevent the consistent creation of a clean Rayleigh wave. It should also be emphasised that our goal is not to perfectly mimic a real-world experiment, but instead to establish the underlying principles of wave interaction with surface roughness. All of these features were defined on the top surface of a rectangular block, while all other surfaces and the volume of the domain were left unaffected.

Obtaining statistically and ergodically meaningful results requires averaging the attenuation coefficient values over multiple simulations, with identical statistical roughness parameter values but unique rough surface profiles. This can create significant computational burden, especially for 3D simulations. As a result, the dimensions of the FE domain were selected dynamically based on the frequency (hence, wavelength) of the simulation and Λ , instead of being fixed, to create a model with the minimum possible volume while ensuring adequate spacing for the source, monitor, and rough and absorbing layer regions. The dimensions of the FE domain are also included in the schematic of Figure 2.

As shown in Figure 2, the dynamic model sizing was implemented by defining the size of the domain to be a function of the wavelength and the correlation length; a script would accept the frequency and correlation length as an input and then calculate the suitable domain size, as per the dimensions shown in Figure 2, which was subsequently used to generate a mesh of that size. Namely, absorbing layers with a thickness equal to $3\lambda_R$ were defined around the FE domain, to absorb any unwanted reflections [23, 24], where λ_R is the Rayleigh wavelength. Additionally, the theory in [7] and [9] assumes a space of infinite extent in both the x and y directions, and therefore, the addition of absorbing layers around the model more closely models this scenario. A

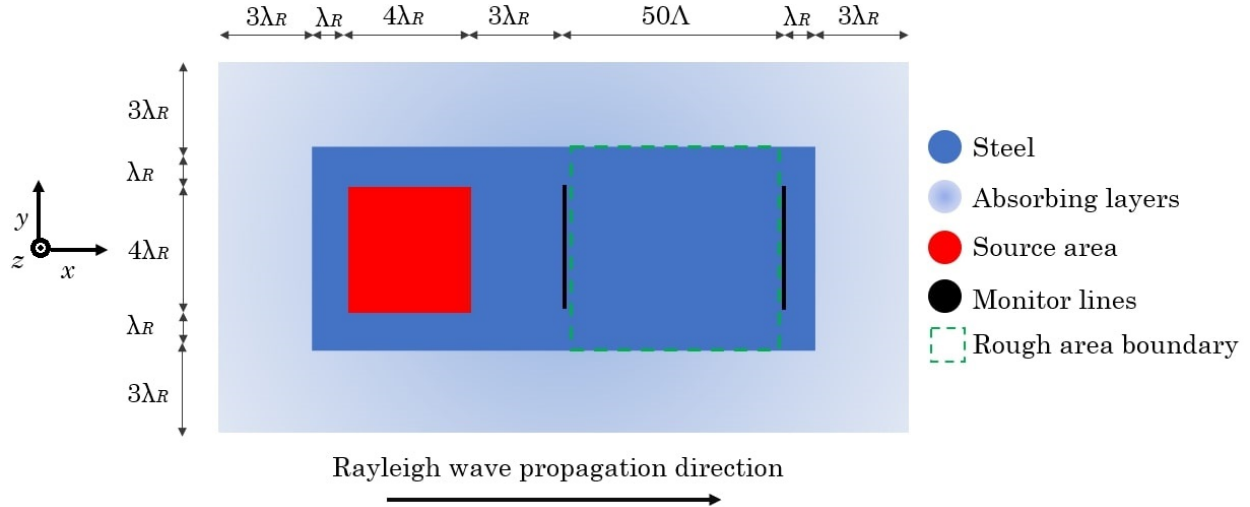


Figure 2: (Colour online) Schematic of the planar view of the FE model, showing the dimensions of the domain as well as the source and rough areas, monitor lines and absorbing regions.

square source area, with side length equal to $4\lambda_R$ was defined at a distance of one λ_R from the right edge of the left absorbing layer; the size of this gap was measured from the left edge of the source square, and not its centre, as demonstrated in Figure 2. Then the monitor line before the rough surface was placed at a distance of $3\lambda_R$ from the right edge of the source area. The length of the rough surface itself was set to be at least equal to 50Λ , as advised by [1]. Another monitor line was placed just after the rough surface, and then, after a gap of length equal to λ_R , a $3\lambda_R$ thick absorbing layer was defined. For the width of the domain, a λ_R gap was defined above and below the source area, followed again by $3\lambda_R$ thick absorbing layers. The thickness of the domain (z direction), was set to be at least $3\lambda_R$, so that the boundary opposite the source area (i.e. the top boundary) would not interfere with the Rayleigh wave.

By following this approach, where all dimensions of the domain were not absolute but rather were determined by the particular frequency and correlation length that were used each time, it was possible to create the minimum possible model size for each particular roughness/frequency case, reducing the computational expense of our simulations. A typical, moderately sized model was of the order of 5.5×10^7 degrees of freedom, and required approximately

6-8 min to solve using three Nvidia (Santa Clara, CA) RTX 2080 Ti cards, with 11GB of memory each.

Steel was used for all simulations (Young’s modulus, $E = 200$ GPa, density, $\rho = 7800$ kg/m³ and Poisson’s ratio, $\nu = 0.29$) with longitudinal wave speed $C_L = 5797$ m/s and shear wave speed $C_T = 3153$ m/s. The Rayleigh wave speed, calculated from the approximation in [19, 25] was found to be 2915 m/s. Here, it is worth noting that the material choice is not expected to affect the asymptotic power relationships, as the theory suggests that they are independent of it.

To create the rough surface, we utilised Pogo’s ability to take an undeformed, cuboid mesh and warp it into the desired shape. To achieve this, the initial model, a 2D warping map and some alignment information are used. Let $z_{(x,y)}$ be the lowest (or highest), undeformed z value of the mesh at a given (x, y) location, and $z'_{(x,y)}$ be the lowest (or highest) desired value, (in our case rough surface value) at the same location. The warping factor at that location, $w_{(x,y)}$ can be calculated by:

$$w_{(x,y)} = \frac{z'_{(x,y)}}{z_{(x,y)}}. \quad (10)$$

For $w_{(x,y)} > 1$, the nodes are extruded away from the reference plane, whereas for $w_{(x,y)} < 1$, the nodes are compressed toward the reference plane, as shown in Figure 3. It is worth noting that if $w_{(x,y)} = 1$, there is no change in the location of the nodes during the warping. When these values are calculated for all (x, y) locations in the mesh, a 2D warping map, containing the respective warping factor values is obtained. Then, the warping map is aligned with the reference plane, i.e. the plane where all $z_{(x,y)}$ values were measured from, and, according to the values of the map, the nodes of the model are either compressed towards the volume of the material, or extended away from it.

When this map contains values corresponding to a 2D projection of a 3D rough surface, it creates a mesh that is locally rough, within the bounds shown in Figure 2. An illustration of this process is shown in Figure 4.

In subfigure 4a the lowest z position of an undeformed mesh is plotted at each (x, y) location; as the mesh is undeformed, and in the shape of a cuboid, all

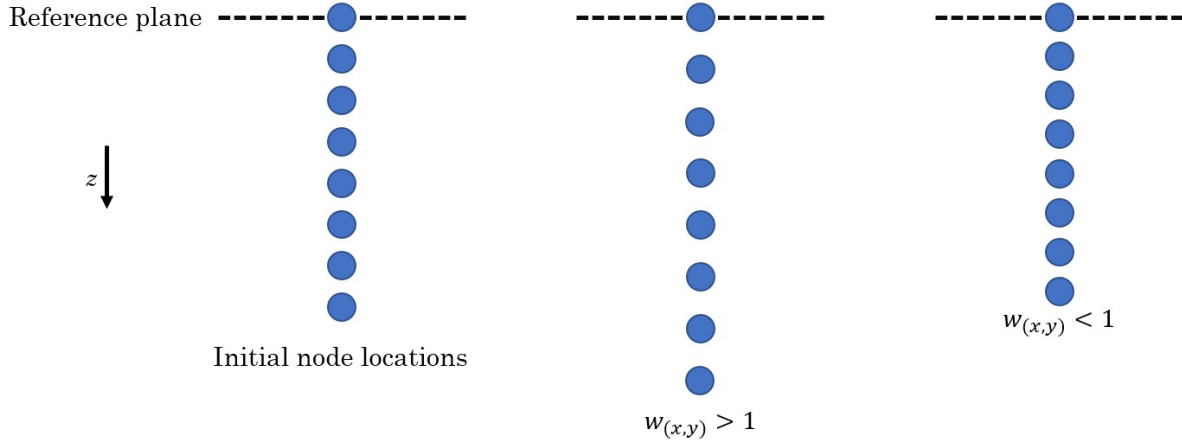


Figure 3: (Colour online) Schematic showing the z position of nodes at an arbitrary (x, y) location, prior to warping (a), for $w_{(x,y)} > 1$ (b) and $w_{(x,y)} < 1$ (c).

points have the same z value. Subfigure 4b shows the matrix which contains the values determining the desired final z position - those warping factor values are given as a ratio between the final and the initial position as per Equation (10). A value of this ratio greater than one indicates extrusion, while a value smaller than one indicates compression.

Also, given that we required our model to only be rough within a pre-defined area, as shown in Figure 2, we populated the warping factor matrix in subfigure 4b with ones everywhere besides the desired rough region. Then, subfigure 4c shows the lowest z position of a deformed mesh at each (x, y) location, where the deformation has occurred as instructed by the warping factor map in subfigure 4b; the resulting z value at each point in subfigure 4c is simply the result of multiplying the respective value in subfigure 4a with the respective warping factor in subfigure 4b. In the FE domain, the mesh in each (x, y) location is warped by displacing the nodes from their initial position, according to the value of the warping factor at each location, distorting the mesh to achieve the desired z value at that location.

In terms of the excitation, it was desirable to excite a clean Rayleigh wave signal on the bottom surface of the block, with distinguishable peaks for the purposes of attenuation calculations, and with minimal excitation of other modes, as those could interfere with the attenuation measurements. We

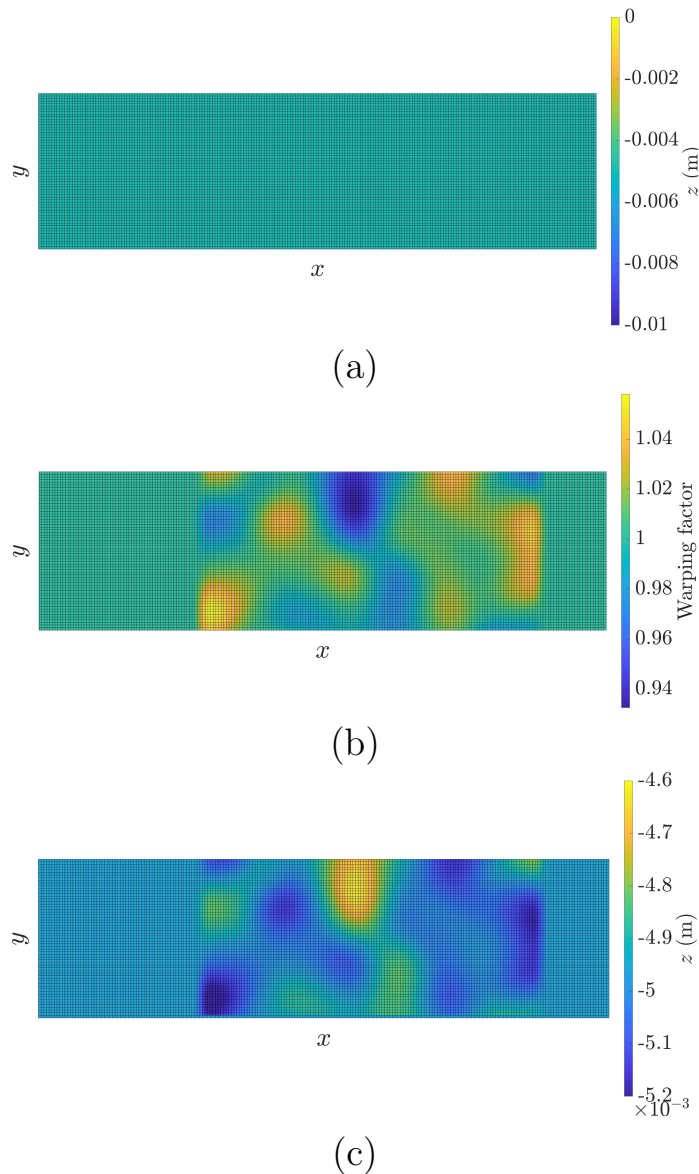


Figure 4: (Colour online) Illustration of the process used to create the rough surfaces by deforming a cuboid mesh with an initially flat boundary to the desired shape. In (a) we are plotting the z values of the lowest-most points in an undeformed, cuboid mesh, at each (x, y) location; as this is undeformed, all points lie in the same plane. Subfigure (b) shows the warping factor map, which when multiplied by the values in (a) warps them into the shape shown in (c). All nodes not belonging to (a), are displaced accordingly, i.e. each “column” of nodes located above a (x, y) location is either stretched or compressed according to the warping factor in (b) to achieve the result in (c).

managed to achieve this in our prior work [10] and therefore, we used an extension of this method here. In the method in [10], two time-harmonic signals, with a 90° phase shift were assigned to each of the source nodes (i.e. a sine and a cosine signal). The complex amplitude, a_i , assigned to the i th source node, located at the x_i position is given by:

$$a_i = \frac{1}{2} \left[1 - \cos \left(2\pi \frac{x_i - x_{\min}}{x_{\max} - x_{\min}} \right) \right] e^{jqx_i}, \quad (11)$$

where, x_{\min} is the position of the leftmost source node, x_{\max} is the position of the rightmost source node and j is the imaginary unit. In the 2D model, the first signal was applied to each node with a weight of $[\Im(a_i) - \Re(a_i)]$, while the cosine signal was applied with a weighting of, $[-\Re(a_i) - \Im(a_i)]$ where the first and second entries in the previous vectors denote the x and y directions respectively.

For extending this to the 3D model, we applied the same amplitude window to each of the individual source lines that composed the source area; this is analogous to “extruding” this window in the y direction, i.e.

$$a_{(i,j)} = \frac{1}{2} \left[1 - \cos \left(2\pi \frac{x_i - x_{\min}}{x_{\max} - x_{\min}} \right) \right] e^{jqx_i}, \quad (12)$$

where $a_{i,j}$ is the amplitude assigned to the i th node of the j th row of the source line. The result was a clean Rayleigh wave, travelling in the positive x direction, with minimal excitation of other modes. In this case, each of the two signals was applied to each node with a weight of $[\Im(a_i) - \Re(a_i) \ 0]$, while the cosine signal was applied with a weighting of, $[-\Re(a_i) - \Im(a_i) \ 0]$, in the x , y and z directions respectively.

Monitor lines were defined to record the signal before and after the rough surface. The signals received at the monitor lines, either before or after, were summed across each line, and normalised by the number of nodes comprising each line. Finally, the attenuation coefficient was calculated from:

$$\alpha = -\frac{1}{x_r} \ln \left(\frac{A_2}{A_1} \right), \quad (13)$$

where x_r is the distance between the monitor lines, and A_1 and A_2 are the amplitudes of the fast-Fourier transforms of the normalised signals before and after the rough surface respectively.

4 Results and discussion

This section presents the power relationships between α and δ , Λ and f , obtained by processing the FE results, in all three scattering regimes. To obtain statistically and ergodically stable results, it was necessary to perform Monte Carlo simulations with multiple realisations of surfaces with the same statistical parameter values but unique $h(x, y)$ profiles, for each roughness case. As a result, each of the data points presented in subsequent figures in subsections 4.1, 4.2 and 4.3 is the ensemble average of 30 realisations. Standard error (SE) bars are also plotted for each data point, where SE is defined as:

$$\text{SE} = \frac{\sigma}{\sqrt{N}}, \quad (14)$$

where σ is the standard deviation of N attenuation values, obtained from N realisations.

This number of realisations was deemed sufficient for the purpose of our study, in all scattering regimes, as a convergence study showed that the value of the attenuation coefficient had converged prior to the 30 realisation limit. An example of a convergence plot, illustrating the evolution of the ensemble average attenuation coefficient, at three roughness scenarios (each corresponding to one of the three scattering regimes) is shown in Figure 5.

As shown in Figure 5, the attenuation coefficient appears to have converged within 30 realisations; this relatively fast convergence of ensemble averaging is due to the fact that the length and width of the rough area was large enough for fairly efficient spatial averaging even without significant ensemble averaging. Therefore, this number was judged to be sufficient for the purposes of our study.

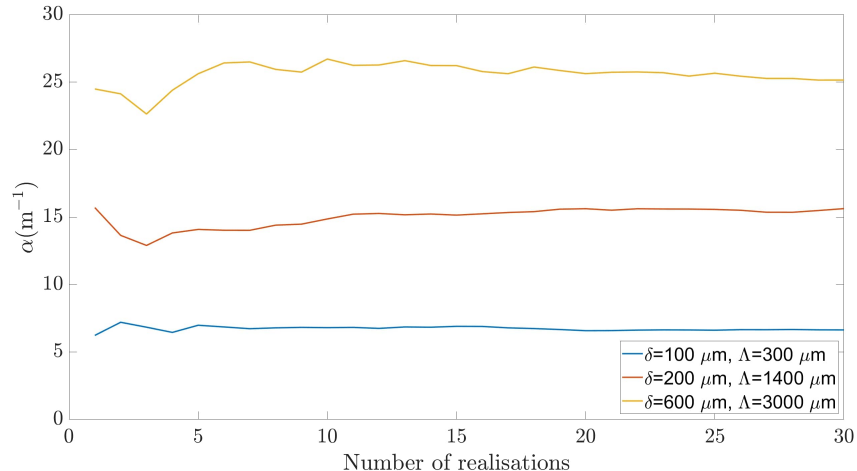


Figure 5: (Colour online) Variation of the attenuation coefficient, as the number of realisations increases, for three roughness scenarios. The central frequency of the simulation results presented here is 1 MHz. The blue, orange and yellow lines correspond to results belonging to the Rayleigh, stochastic and geometric regimes respectively.

4.1 Rayleigh regime

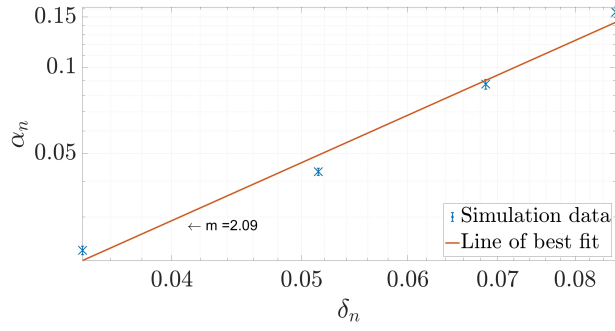
As discussed in Section 2, in the Rayleigh regime, we expect $\alpha_R \propto \delta^2 \Lambda^2 f^5$. For uniformity with our work in [10], we plot the FE results in their normalised form where possible, i.e. we plot α_n vs δ_n , and α_n vs Λ_n , where $\alpha_n = \alpha \lambda_R$, $\delta_n = \delta / \lambda_R$, $\Lambda_n = \Lambda / \lambda_R$, and λ_R is calculated at the central frequency of the simulation. This does not affect the power relationship between α and either δ or Λ , as all simulations in the respective figure are completed at the same frequency, and therefore, all values are normalised by the same constant. For asymptotic analysis relating to f , we are plotting against absolute values; this is because the frequency is not constant in this case, and therefore the wavelength varies.

The results relating to the Rayleigh regime are shown in Figure 6, with the results relating to δ , Λ and f shown in 6a, 6b and 6c respectively. For investigating the δ^2 relationship, Λ was fixed to 400 μm , f was set to 1 MHz ($\lambda_R = 2.92$ mm), and δ was varied from 100 μm to 250 μm . This normalisation value ($\lambda_R = 2.92$ mm) was used in all subsequent analysis where the frequency was kept constant, as all such simulations used a Hann-

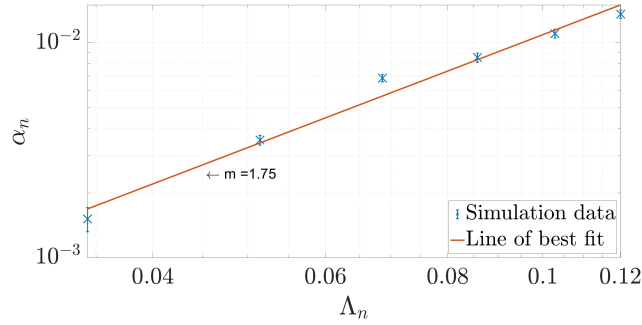
windowed signal with a central frequency of 1 MHz. The gradient of the best fit line, on a log-log scale, in subfigure 6a is 2.09, which is close to the theoretical value of 2. For the Λ^2 relationship, δ was fixed to 100 μm , f was set again to 1 MHz and Λ was varied from 100 μm to 350 μm . The gradient of the best fit line from this set of simulations, as shown in subfigure 6b was found to be 1.75 which is again close to the theoretical value. Finally, for the f^5 relationship, the statistical parameters of the random rough surfaces were set to $\delta = 100\mu\text{m}$ and $\Lambda = 300\mu\text{m}$, while f was varied from 0.7 MHz to 1.2 MHz. (λ_R varying from 4.16 mm to 2.43 mm). As shown in subfigure 6c, a gradient of 5.00 was retrieved from the best fit line.

It appears that the FE results match the theory closely, for all three power relationships. In this regime, as discussed in Section 2, $\omega_2 \propto (\omega\Lambda)^4$, which when substituted in Equation (8) yields the $\delta^2\Lambda^2f^5$ proportionality; physically, in the low frequency limit of this regime, the wavelength becomes so large compared with the features of the rough surface, that the rough surface appears flat to the Rayleigh wave, and the attenuation coefficient tends to zero.

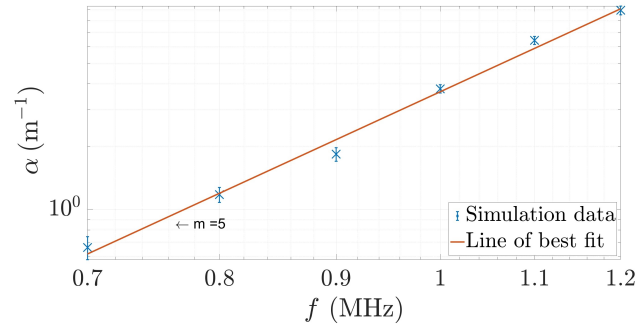
Here it is important to add that a beamspread correction was applied to these results. The theory in [7] assumes a plane wave for the derivations. We have found that a square source with a side length of $4\lambda_R$ was sufficiently close to a plane wave source, however, in the Rayleigh regime, where the attenuation values are small, the small beamspread effect was no longer negligible. To account for this, a model with no roughness was run for each frequency and x_r case, and the beamspread was converted into an equivalent attenuation coefficient, which was then subtracted from the value obtained from each rough model, to give the true α value. There is no roughness-induced attenuation in a flat model, therefore, any loss in Rayleigh wave amplitude is solely due to beamspread. The principle of similitude, as discussed in this context in [10], implies that the rough case must suffer the same loss in amplitude due to beamspread, in addition to the attenuation caused by the roughness. For the frequencies presented here (0.7 MHz to 1.2 MHz), the beamspread correction values were in the range from 0.91 m^{-1} to 2.96 m^{-1} .



(a)



(b)



(c)

Figure 6: (Colour online) FE results, relating to the Rayleigh regime. The figure shows the FE results, plotted as \times , and the line of best fit through them. The gradient of the best fit line, m , is also shown. Values of the attenuation coefficient, either absolute or normalised, are plotted on the vertical axis, while the variable whose power relationship is investigated (δ_n , Λ_n and f in (a), (b) and (c) respectively) is plotted on the horizontal axis.

4.2 Stochastic regime

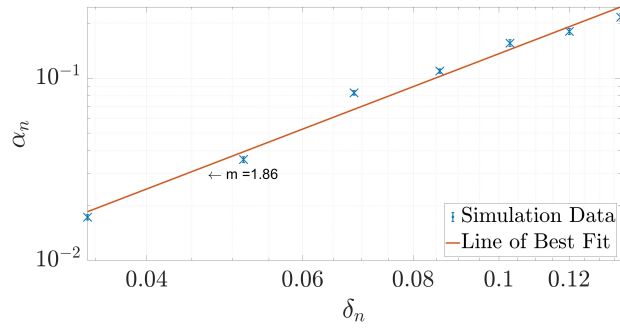
In the stochastic regime, the theory predicts that $\alpha_S \propto \delta^2 \Lambda^{-1} f^2$. The FE results relating to the stochastic regime are shown in Figure 7, with the results relating to δ , Λ and f shown in subfigures 7a, 7b and 7c respectively. For the investigation of the δ^2 relationship, Λ was fixed to $800 \mu\text{m}$, f was set to 1 MHz and δ was varied from $100 \mu\text{m}$ to $400 \mu\text{m}$. For the Λ^{-1} relationship, δ was fixed to $200 \mu\text{m}$, f was set to 1 MHz and Λ was varied from $800 \mu\text{m}$ to $1600 \mu\text{m}$. Finally, for the f^2 relationship, δ and Λ were fixed to $200 \mu\text{m}$ and $800 \mu\text{m}$ respectively, while f was varied from 0.8 MHz to 1.8 MHz (λ_R varying from 3.64 mm to 1.62 mm).

The gradients of the best fit lines were found to be 1.86, -1.06 and 2.15 for δ , Λ and f respectively, all of which agree well with the values proposed by the theory. This shows that our model was able to retrieve all the power relationships in the stochastic regime too.

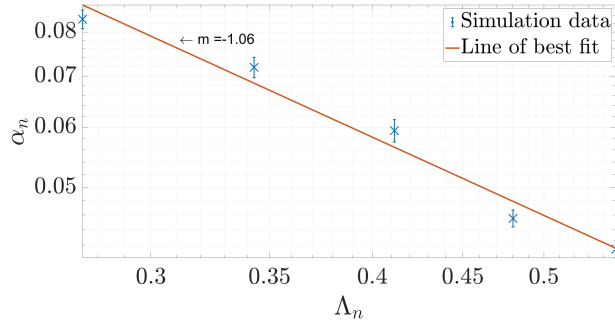
4.3 Geometric regime

In the geometric regime, the theory predicts that $\alpha_G \propto \Lambda^{-1}$, with the attenuation coefficient being independent of δ and f . The results relating to the geometric regime are shown in Figure 8. For the investigation of this power relationship, δ and f were fixed at $600 \mu\text{m}$ and 1 MHz respectively, and Λ was varied from $2000 \mu\text{m}$ to $3000 \mu\text{m}$.

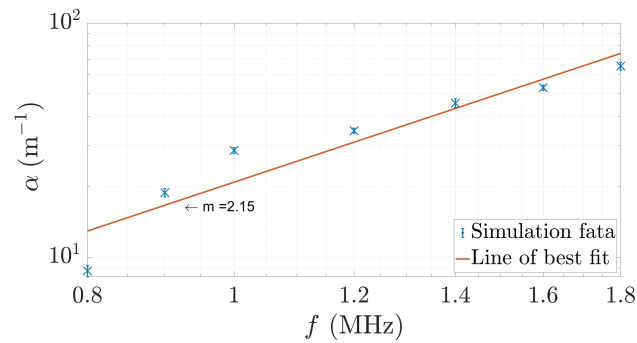
As shown in subfigure 8b, the inverse proportionality between the attenuation coefficient and the correlation length is demonstrated well by our FE results, as the gradient of the best fit line is -0.93. This shows that our model is able to encapsulate the physical phenomena of the geometric scattering well; in the geometric regime, the wavelength has become so short that the only important metric in the scattering is the number of peaks/troughs, and not their size, as the wave can traverse their height without getting scattered from them. A long correlation length implies fewer obstacles, and therefore, the attenuation coefficient reduces with an increase in correlation length. This is also reflected in the power relationships relating to δ (subfigure 8a) and f (subfigure 8c), which have both significantly diminished, from their value of 2 in the stochastic region, to values closer to zero.



(a)

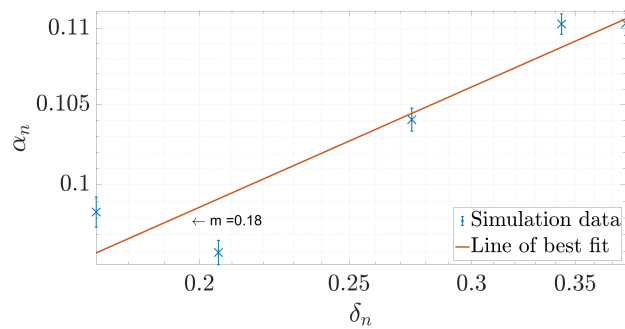


(b)

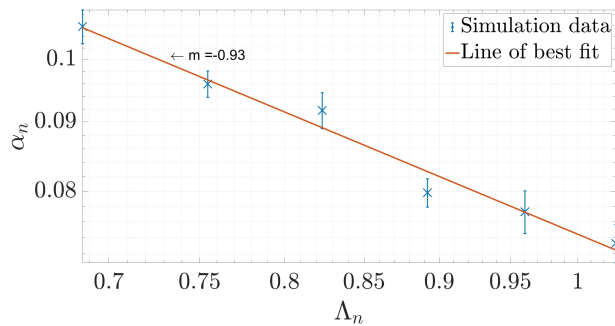


(c)

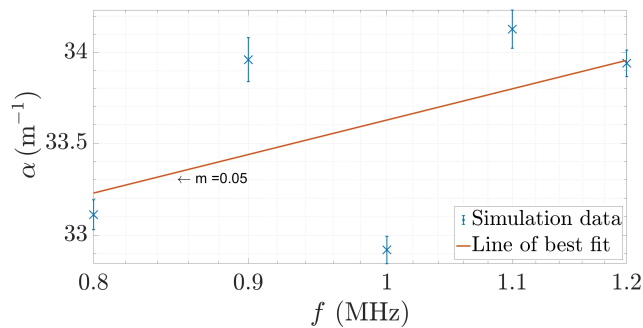
Figure 7: (Colour online) FE results, relating to the stochastic regime. The figure shows the FE results, plotted as \times , and the line of best fit through them. The gradient of the best fit line, m , is also shown. Values of the attenuation coefficient, either absolute or normalised, are plotted on the vertical axis, while the variable whose power relationship is investigated (δ_n , Λ_n and f in (a), (b) and (c) respectively) is plotted on the horizontal axis.



(a)



(b)



(c)

Figure 8: (Colour online) FE results, relating to the geometric regime. The figure shows the FE results, plotted as \times , and the line of best fit through them. The gradient of the best fit line, m , is also shown. Values of the attenuation coefficient, either absolute or normalised, are plotted on the vertical axis, while the variable whose power relationship is investigated (δ_n , Λ_n and f in (a), (b) and (c) respectively) is plotted on the horizontal axis.

4.4 Summary of results

A summary of our results, compared with the theoretical asymptotic power relationships is shown in Table 2.

Table 2: Comparison between expected (theoretical) and FE asymptotic power relationships, between the attenuation coefficient and the RMS height, correlation length and frequency.

Regime	Rayleigh	Stochastic	Geometric
Limits	$q\delta < q\Lambda < 1$	$q\delta < 1 < q\Lambda$	$1 < q\delta \ll q\Lambda$
$\alpha(\delta, \Lambda, f)$ (Theory)	$\delta^2 \Lambda^2 f^5$	$\delta^2 \Lambda^{-1} f^2$	Λ^{-1}
$\alpha(\delta, \Lambda, f)$ (FE)	$\delta^{2.09} \Lambda^{1.75} f^{5.00}$	$\delta^{1.86} \Lambda^{-1.06} f^{2.26}$	$\Lambda^{-0.93}$

As shown in Table 2, in the Rayleigh regime, the powers of δ , Λ and f were 4.5%, -12.5% and 0.0 % away from the theoretical value respectively. For the stochastic regime, the same differences for the same variables were equal to 7.0%, 6.0%, and 13.0%, while for the power of Λ in the geometric regime the difference was found to be 7.0%. Overall, we were able to achieve good agreement between our FE results and the theoretical asymptotic power relationships, in all scattering regimes. Also, we were able to show that the power relationships hold true and preserve their theoretical value even in cases where the statistical parameters fall outside the region of validity of the theory, i.e. for cases when $\delta/\Lambda > 0.3$ [7].

5 Conclusion

In this work, we have completed a study of the asymptotic behaviour of the attenuation coefficient of a Rayleigh wave with respect to the RMS height and correlation length of a statistically rough surface, and the wave's frequency. Results were obtained in all three scattering regimes (Rayleigh, stochastic and geometric), using high-fidelity FE modelling. By utilising the findings in our previous work in [10], we were now able to complete this investigation in 3D space.

We found good agreement between our results and the values proposed by the theory in all scattering regimes. As FE modelling makes no further assumptions apart from the discretisation of the domain into finite areas/volumes, and the approximation of derivatives as quotients, it provides robust further insight to the theory, that has been derived under different assumptions. Additionally, we were able to provide further confidence to the Λ^{-1} relationship between the attenuation coefficient and the correlation length, which was an unknown variable in our previous work. Our results also extended to roughness scenarios which lie outside the regions of validity of the small perturbation theory, showing that the power relationships hold true even in those.

By utilising FE modelling we were able to obtain these results under a unified approach, as we used the same FE modelling techniques regardless of the scattering regime. This contrasts with previous theoretical work, which requires different mathematical tools and approaches, tailored to the scattering regime being investigated. Also, FE modelling removes the necessity of a priori knowledge of the ω_2 function proposed in [7], which is complicated to calculate, unique to each roughness/material case and potentially impractical to use in a realistic environment. Additionally, 3D modelling removes the need for using analogies between 2D and 3D theory, and allows for direct investigation of real-world scenarios. Finally, this agreement between FE modelling and the existing theory lays the foundation for potentially using solely FE results for attenuation coefficient predictions for roughness cases where the theory is limited and experimental measurement is difficult.

In terms of NDE applications, if the statistical parameters characterising a surface are known, FE modelling can be used to predict the corresponding attenuation coefficient, and hence apply corrections to experimental measurements; such a capability has been demonstrated here, as it is possible to replace the random rough surfaces used in our study with rough surfaces obtained experimentally. This can be useful for cases where attenuation is used as an NDE metric. For instance it is possible to use attenuation for fatigue state characterisation [3, 26, 27], however, the presence of roughness would result in higher attenuation values than what can solely be attributed to fatigue, and thus erroneous fatigue life predictions. Additionally, an “inverted” approach could be used where an experimentally measured attenuation coeffi-

cient is resolved into the corresponding severity of surface roughness. Such an assessment is important for parts made with additive manufacturing, as their layer-by-layer creation results in inherent surface roughness [28–31], which affects their performance [32–34]. Results for both examples are attainable with the existing theory, however, the FE method presented here removes the low-roughness restriction imposed by it, and allows for the prediction of the attenuation coefficient in a unified approach, regardless of the magnitude of the scattering regime and the statistical parameters characterising the rough surface. Finally, numerical modelling can quite readily handle cases where the roughness exists on curved components (e.g. shot-peened cylindrical shafts), for which currently there are no theoretical models predicting the attenuation coefficient.

6 Author Declaration

The authors have no conflicts of interest to disclose.

The data is available on request from the authors.

Georgios Sarris was funded by the UK Research Centre in Nondestructive Evaluation , iCASE number 17000191, with contributions from Rolls-Royce Holdings plc and Jacobs Engineering Group Inc.

References

- [1] J. A. Ogilvy, *Theory of wave scattering from random rough surfaces*. CRC Press, 1991.
- [2] S. Kenderian, T. P. Berndt, R. E. Green, and B. B. Djordjevic, “Ultrasonic monitoring of dislocations during fatigue of pearlitic rail steel,” *Materials Science and Engineering: A*, vol. 348, no. 1-2, p. 90–99, 2003.
- [3] T. Ohtani, K. Nishiyama, S. Yoshikawa, H. Ogi, and M. Hirao, “Ultrasonic attenuation and microstructural evolution throughout tension–compression fatigue of a low-carbon steel,” *Materials Science and Engineering: A*, vol. 442, no. 1, p. 466–470, 2006.
- [4] B. Yan, Y. Song, S. Nie, M. Yang, and Z. Liu, “Measurement of the acoustic non-linearity parameter of materials by exciting reversed-phase Rayleigh waves in opposite directions,” *Sensors*, vol. 20, no. 7, p. 1955, 2020.
- [5] C. Zhang and J. D. Achenbach, “Dispersion and attenuation of surface waves due to distributed surface-breaking cracks,” *The Journal of the Acoustical Society of America*, vol. 88, no. 4, p. 1986–1992, 1990.
- [6] A. A. Maradudin and D. L. Mills, “The attenuation of Rayleigh surface waves by surface roughness,” *Annals of Physics*, vol. 100, no. 1-2, pp. 262–309, 1976.
- [7] A. G. Eguiluz and A. A. Maradudin, “Frequency shift and attenuation length of a Rayleigh wave due to surface roughness,” *Physical Review B*, vol. 28, no. 2, p. 728, 1983.
- [8] V. N. Chukov, “Rayleigh wave scattering by statistical arbitrary form roughness,” *Solid State Communications*, vol. 149, pp. 7827–7839, 2009.
- [9] V. V. Kosachev, Y. V. Lokhov, and V. N. Chukov, “Theory of attenuation of Rayleigh surface acoustic waves on a free randomly rough surface of a solid,” *Journal of Experimental and Theoretical Physics*, vol. 67, pp. 1825–1830, 1988.

- [10] G. Sarris, S. G. Haslinger, P. Huthwaite, P. B. Nagy, and M. J. S. Lowe, “Attenuation of Rayleigh waves due to surface roughness,” *The Journal of the Acoustical Society of America*, vol. 149, no. 6, p. 4298–4308, 2021.
- [11] A. V. Pamel, P. B. Nagy, and M. J. S. Lowe, “On the dimensionality of elastic wave scattering within heterogeneous media,” *The Journal of the Acoustical Society of America*, vol. 140, pp. 4360–4366, 2016.
- [12] L. Yang, O. Lobkis, and S. Rokhlin, “An integrated model for ultrasonic wave propagation and scattering in a polycrystalline medium with elongated hexagonal grains,” *Wave Motion*, vol. 49, no. 5, p. 544–560, 2012.
- [13] A. V. Pamel, *Ultrasonic inspection of highly scattering materials*. PhD thesis, Imperial College London, 2015.
- [14] J. A. Ogilvy, “Computer simulation of acoustic wave scattering from rough surfaces,” *Journal of Physics D: Applied Physics*, vol. 21, pp. 260–277, 1988.
- [15] F. Shi, M. J. S. Lowe, X. Xi, and R. V. Craster, “Diffuse scattered field of elastic waves from randomly rough surfaces using an analytical Kirchhoff theory,” *Journal of the Mechanics and Physics of Solids*, vol. 92, pp. 260–277, 2016.
- [16] J. Zhang, B. W. Drinkwater, and P. D. Wilcox, “Longitudinal wave scattering from rough crack-like defects,” *IEEE Transactions on Ultrasonics, Ferroelectrics, and Frequency Control*, vol. 58, no. 10, pp. 2171–2180, 2011.
- [17] W. Choi, F. Shi, M. J. S. Lowe, E. A. Skelton, R. V. Craster, and W. L. Daniels, “Rough surface reconstruction of real surfaces for numerical simulations of ultrasonic wave scattering,” *NDT & E International*, vol. 98, p. 27–36, 2018.
- [18] Q. Chen and N. Wong, “New simulation methodology of 3D surface roughness loss for interconnects modelling,” in *Design, Automation & Test in Europe Conference & Exhibition*, 2012.

- [19] J. D. Achenbach, *Wave propagation in elastic solids*. North Holland Publishing Company, 1973.
- [20] J. L. Rose, *Ultrasonic guided waves in solid media*. Cambridge University Press, 2014.
- [21] P. Huthwaite, “Accelerated finite element elastodynamic simulations using the GPU,” *Journal of Computational Physics*, vol. 257, p. 687–707, 2014.
- [22] K. J. Bathe, *Finite Element Procedures*. Prentice-Hall, 1996.
- [23] P. Rajagopal, M. Drozd, E. A. Skelton, M. J. S. Lowe, and R. V. Craster, “On the use of absorbing layers to simulate the propagation of elastic waves in unbounded isotropic media using commercially available finite element packages,” *NDT & E International*, vol. 51, p. 30–40, 2012.
- [24] J. Pettit, A. Walker, P. Cawley, and M. Lowe, “A stiffness reduction method for efficient absorption of waves at boundaries for use in commercial finite element codes,” *Ultrasonics*, vol. 54, no. 7, p. 1868–1879, 2014.
- [25] I. A. Viktorov, *Rayleigh and Lamb Waves (Translated from Russian)*. Plenum Press, 1967.
- [26] T. Ohtani, H. Ogi, Y. Minami, and M. Hirao, “Ultrasonic attenuation monitoring of fatigue damage in low carbon steels with electromagnetic acoustic resonance (EMAR),” *Journal of Alloys and Compounds*, vol. 310, no. 1, p. 440–444, 2000.
- [27] G. Sarris, S. G. Haslinger, P. Huthwaite, and M. J. S. Lowe, “Ultrasonic methods for the detection of near surface fatigue damage,” *NDT & E International*, vol. 135, p. 102790, 2023.
- [28] A. Boschetto, L. Bottini, and L. Venial, “Surface roughness and radiusing of Ti6Al4V selective laser melting-manufactured parts conditioned by barrel finishing,” *The International Journal of Advanced Manufacturing Technology*, vol. 94, pp. 2773–2790, 2018.

- [29] A. Boschetto, L. Bottini, and L. Venial, “Roughness modeling of AlSi10Mg parts fabricated by selective laser melting,” *Journal of Materials Processing Technology*, vol. 241, pp. 154–163, 2017.
- [30] T. Zhang and L. Yuan, “Understanding surface roughness on vertical surfaces of 316 L stainless steel in laser powder bed fusion additive manufacturing,” *Powder Technology*, vol. 411, p. 117957, 2022.
- [31] H. Rezaeifar and M. Elbestawi, “Minimizing the surface roughness in l-pbf additive manufacturing process using a combined feedforward plus feedback control system,” *The International Journal of Advanced Manufacturing Technology*, vol. 121, no. 11-12, p. 7811–7831, 2022.
- [32] A. Yadollahi, M. Mahtabi, A. Khalili, H. Doude, and J. Newman, “Fatigue life prediction of additively manufactured material: Effects of surface roughness, defect size, and shape,” *Fatigue Fracture of Engineering Materials and Structures*, vol. 41, no. 7, p. 1602–1614, 2018.
- [33] J. Gockel, L. Sheridan, B. Koerper, and B. Whip, “The influence of additive manufacturing processing parameters on surface roughness and fatigue life,” *International Journal of Fatigue*, vol. 124, p. 380–388, 2019.
- [34] H. Masuo, Y. Tanaka, S. Morokoshi, H. Yagura, T. Uchida, Y. Yamamoto, and Y. Murakami, “Influence of defects, surface roughness and hip on the fatigue strength of ti-6al-4v manufactured by additive manufacturing,” *International Journal of Fatigue*, vol. 117, p. 163–179, 2018.